Reactive vapor-phase dealloying-alloying turns oxides into sustainable bulk nano-structured porous alloys

Shaolou Wei[1,*], Yan Ma[1, 2], and Dierk Raabe[1,*]

[1.] *Max-Planck Institute for Sustainable Materials, Max-Planck-Straße 1, Düsseldorf 40237, Germany*

[2.] *Delft University of Technology, 2,2628 CD, Netherlands*

*Corresponding author: d.raabe@mpie.de (Dierk Raabe) or sl.wei@mpie.de (Shaolou Wei)

Abstract

For millennia, *alloying* has been the greatest gift from metallurgy to humankind: a process of mixing elements, propelling our society from the Bronze Age to the Space Age. *Dealloying*, by contrast, acts like a penalty: a corrosive counteracting process of selectively removing elements from alloys or compounds, degrading their structural integrity over time. We show in this study that when these two opposite metallurgical processes meet in a reactive vapor environment, profound sustainable alloy design opportunities become accessible, enabling bulk nano-structured porous alloys directly from oxides, with zero carbon footprint. We introduce thermodynamically well-grounded treasure maps that turn the intuitive opposition between *alloying* and *dealloying* into harmony, facilitating a quantitative approach to navigate synthesis in such an immense design space. We demonstrate this new alloy design paradigm by synthesizing nano-structured Fe-Ni-N porous martensitic alloys fully from oxides in a single solid-state process step, and substantiating the critical kinetic processes responsible for the desired microstructure. Our approach not only reforms the intuitive conflict between *alloying* and *dealloying*, but also motivates the integration amongst chemical synthesis, extractive, and physical metallurgy to diversify sustainable alloy design.

One sentence highlight:

A thermodynamically guided alloy synthesis paradigm that can directly turn oxides into sustainable bulk nano-structured porous alloys

Since their birth through *alloying*, almost all metallic materials have faced a common adversary, *dealloying*, a corrosive mass transport process that selectively removes the most active constituent under certain boundary conditions (*1–3*), causing microstructural degradation over time. The quantized unit of *dealloying*, individual atom removal from a pre-existing crystal lattice (*4*, *5*), however, sparks the alloy design proposition of our work: oxygen, the most abundant alloying element in the earth's crust and ubiquitous in natural minerals (*6*), may also be removed from a corresponding oxide-containing lattice, if it reveals a higher affinity to the vapor-phase than to its solid-state host lattice (*7*). Such a process, however, is often associated with an excessive energy cost (*e.g.* through the Schottky reaction $\text{Base} \rightarrow V_O^{\cdot\cdot} + V_M''$, where $V_O^{\cdot\cdot}$ stands for the positively-charged oxygen vacancy, and V_M'' for the negatively-charged cation vacancy, following the Kröger-Vink notation), largely due to the ionic bonding nature of the oxides. The most effective approach to overcome this intrinsic penalty is to conceive redox reactions through the vapor-phase, facilitating $O_O^\times \rightarrow \frac{1}{2}O_2 + V_O^{\cdot\cdot} + 2e'$ (where $O_O^\times$ is the charge-neutral oxygen atom residing in the solid-state lattice, and e' the transferred electron, **Fig. 1 A, top**), as has been successfully practiced for decades in tuning the ionic transport properties of functional ceramics (*8–10*) and in the more recent solid-state production of sustainable iron from its ores via H_2 gas (*6*, *11*, *12*). This sort of reactive vapor-phase *dealloying* process phenomenologically mimics the conventional electrochemical dealloying operation (*3*, *5*, *13*) in a sense that it also encourages porous structure creation, but through the migration and agglomeration of oxygen vacancies ($V_O^{\cdot\cdot}$). On the contrary to *dealloying*, *alloying* calls for individual atom addition to a host lattice, either on the substitutional sites or on the interstitial sites. The former case, substitutional alloying, can be fulfilled if sufficient atomic scale mixing (*14*) can be concurrently activated upon or after two or more oxides completely undergo reactive vapor-phase *dealloying* at elevated temperatures. The reactive vapor-phase environment, on the other hand, serves as a natural repository of interstitials, through which nitrogen and carbon can dissolve into the existing alloy via gas-solid reactions (**Fig. 1 A, top**), as supported by the fruitful investigations on gaseous nitriding or carburizing (*15–17*). Altogether, these considerations form the conceptual basis for our proposed reactive vapor-phase dealloying-alloying synthesis route. We will demonstrate this approach by first theoretically assessing the energetics of the critical processes involved.

Starting with oxides, we aim to integrate three principal metallurgical processes in one single solid-state operation (**Fig. 1 A, middle**): *(i)* excessive porosity creation through oxide dealloying (*i.e.* the redox-catalyzed mass loss (*18*)); *(ii)* solid-state substitutional alloying via interdiffusion amongst metallic species; and *(iii)* interstitial alloying by harvesting vapor-phase constituents. The resulting microstructure is expected to be naturally hierarchical and nanostructured, since alloying unlocks the metallurgical treasure of phase transformation (**Fig. 1 A, bottom**), the most viable pathway of multi-scale microstructural modulation. We ground our *a priori* theoretical guideline in thermodynamics and examine the energetics for the critical reactive dealloying-alloying phenomena that are involved. **Fig. 1 B** reveals the *first* thermodynamic *treasure map* that assesses the feasibility of reactive dealloying, exploiting two physical parameters: *(i)* $\Delta G^{\circ}_{\text{oxide}} - \Delta G^{\circ}_{H_2O}$, which quantifies the bulk reducibility of oxides when H_2 serves as the predominant reducing agent, according to the Ellingham-Richardson diagram (*6*, *19*); and *(ii)* $\Delta E^{\text{f}}_{O\text{Vac}}$, the oxygen vacancy ($V_O^{\cdot\cdot}$) formation energy, which describes the easiness of creating the quantized unit

of reactive dealloying, since at the atomic scale our conceived process closely follows: $O_O^{\times} \rightarrow \frac{1}{2}O_2 + V_O^{\cdot\cdot} + 2e'$. Desirable consistency is seen between the bulk reducibility and the energetics of $V_O^{\cdot\cdot}$ formation, identifying Fe, Ni, Co, and Cu as the promising metallic elements that can be fully obtained by dealloying oxygen from their oxides exhibiting the highest valence states.

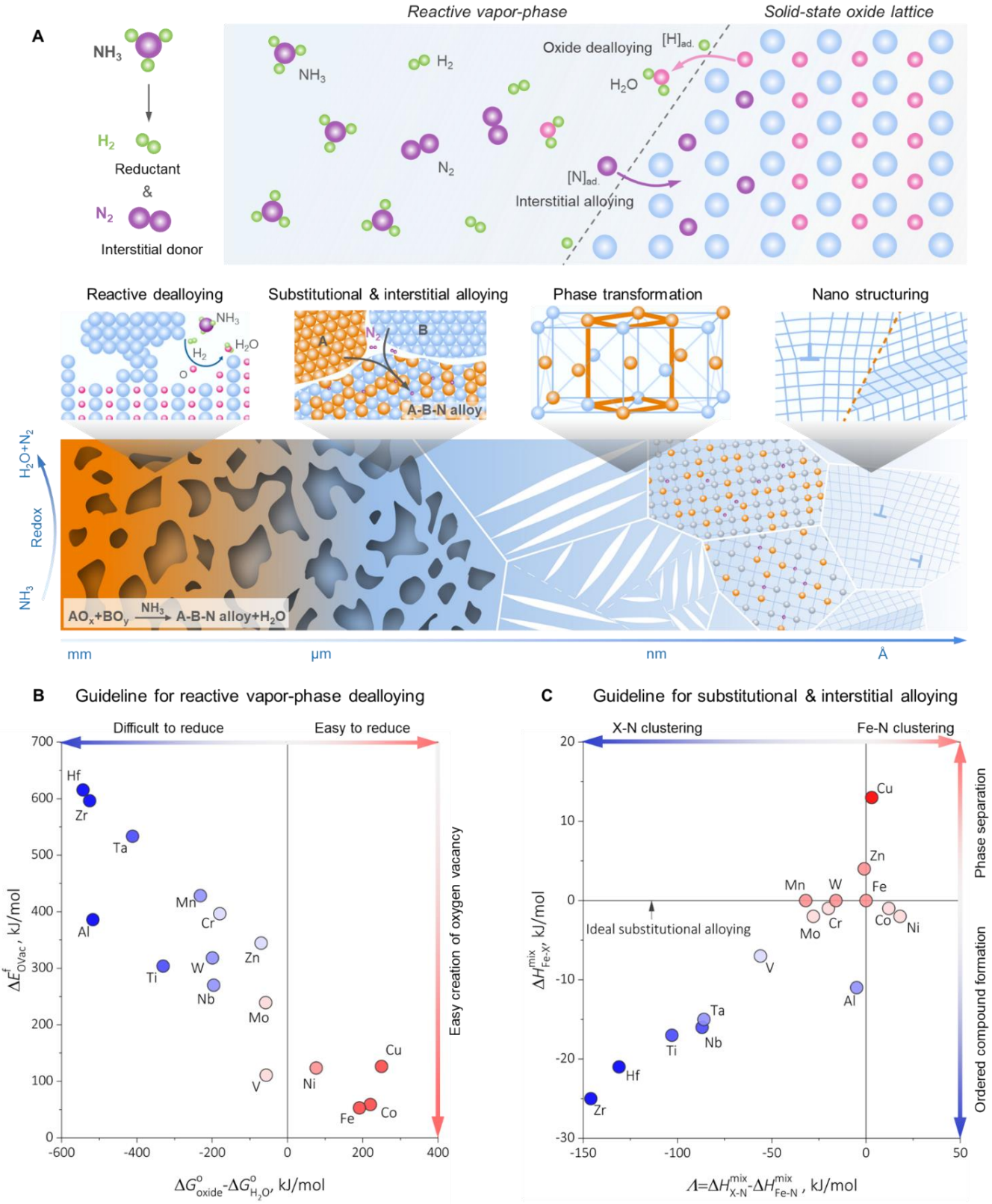

Figure 1 | Thermodynamics-based microstructural design guidelines for reactive vapor-phase dealloying-alloying synthesis. (A) A sketch of the alloy design framework along with multi-scale microstructural evolution micro-events, encompassing reactive dealloying, substitutional alloying, interstitial alloying, phase transformations, and nano structuring. The sketch shows the case of NH_3 as reaction partner for the oxides, providing H_2 as the reductant and N as the interstitial

alloying element. **(B)** The first *thermodynamic treasure map* that assesses bulk oxide reducibility and the easiness of oxygen vacancy creation at the atomic level, guiding reactive dealloying. For simplicity, the $\Delta G^{o}_{oxide} - \Delta G^{o}_{H_2O}$ values were calculated at 700 °C, 1 atm condition for oxides with the highest valence states, using the SGTE thermodynamic database (*20*) and the literature results (*6*, *21*). The ΔE^{f}_{OVac} datum points were collected from the recent ground state density functional theory-based simulations (*22–30*). Complementary thermodynamic considerations of the vapor pressures of pure metallic elements and the boiling points of oxides are further summarized in **Supplementary Fig. 1**. **(C)** The second *thermodynamic treasure map* that quantifies the alloying capability, assuming Fe as the solvent, and N as the interstitial solute. ΔH^{mix}_{Fe-X}, the mixing enthalpy between Fe and the substitutional alloying element X, and the $\Lambda = \Delta H^{mix}_{X-N} - \Delta H^{mix}_{Fe-N}$ values are both computed using the literature data based on the semi-empirical Miedema model (*31*). Physical rationale of the Λ parameters is discussed in discussed greater depth in **Supplementary Note 1**.

To synthesize any bulk alloy, sufficient atomic-scale mixing amongst alloying elements is indispensable, calling the need for a *second* thermodynamic *treasure map* that quantifies alloying capability. Motivated by a carbon-free alloy design framework that exploits NH_3 as the reducing agent (*32*, *33*), we thus conceptualize substitutional and interstitial alloying by presuming Fe as the solvent, nitrogen (N) as the interstitial solute, and opt for two physical parameters (**Fig. 1 C**): *(i)* ΔH^{mix}_{Fe-X}, the mixing enthalpy between Fe and the substitutional solute element X; and *(ii)* $\Lambda = \Delta H^{mix}_{X-N} - \Delta H^{mix}_{Fe-N}$, the mixing enthalpy distinction between X-N and Fe-N, quantifying the propensity of N clustering or nitride formation. The detailed physical foundations of the Λ parameter are rationalized in **Supplementary Note 1**, following the Bragg-Williams mean-field approach (*34*). Alloy compositions residing close to the $\Lambda = 0$ and the $\Delta H^{mix}_{Fe-X} = 0$ lines in **Fig. 1 C** are hence likely to form uniform Fe-X-N solid solutions. The larger positive deviation to the $\Delta H^{mix}_{Fe-X} = 0$ line indicates the stronger tendency of Fe-X phase separation and *vice versa* for Fe-X long-range ordered compound formation. Similarly, the more significant deviation to the $\Lambda = 0$ line implies the more prominent N clustering or nitride formation. In **Supplementary Fig. 1**, we further clarify the potential role of vapor pressure, concluding that the sublimation propensity of Fe, Cu, Ni, and Co is negligible below 800 °C, 1 atm. **Fig. 1 B** and **C** together with **Supplementary Fig. 1** serve as the theoretical basis for our reactive vapor-phase dealloying-alloying synthesis route, which could inspire an immense number of entirely new alloy compositions, synthesized in a single step and under potentially even exothermic conditions. To unambiguously verify this new alloy design paradigm, we choose to synthesize a porous Fe-10Ni-N at. % martensitic alloy using NH_3 as the reducing agent, aiming to demonstrate the four principal microstructural evolution micro-events proposed, encompassing reactive dealloying, substitutional and interstitial alloying, phase transformations, and nano-structuring (**Fig. 1 A**). As sketched in **Fig. 1 A**, Herein, the role of NH_3 is two-fold: *first*, providing the hydrogen to dealloy and hence reduce the oxides, producing H_2O as the only byproduct; and *second*, offering the nitrogen as interstitial alloying element, diversifying solid-state alloy design.

Our synthesis starts with blending together Fe_2O_3 and NiO oxides and cold-compacting them into bulk pellets, targeting an Fe-10 at. % Ni stoichiometry. Secondary electron (SE) micrograph along with energy dispersive X-ray spectroscopy (EDS) maps cross-validate the uniformity of the oxide mixture (**Fig. 2 A**) where no traits of mechanical alloying are observed. Upon heating in an NH_3 atmosphere (**Fig. 2 B**), the pellet starts to exhibit a discernible mass loss at ~455 °C, signifying the inception of reactive dealloying, which aligns with the NH_3 decomposition complete temperature in the literature (*33*, *35*). The

corresponding conversation rate (α) shows a sigmodal-like increasing trend as the reaction progresses, which eventually plateaus at unity, confirming the complete oxygen removal from the oxides. A predominant peak accompanied by a subtle inflection is seen in the $\mathrm{d}\alpha/\mathrm{d}t$ curve, implying stepwise micro-mechanisms of the underlying redox reactions, which will be explored later. The synthesized bulk alloy reveals a silvery metallic appearance, contrasting the hematite red of its oxide counterpart, and *ex situ* synchrotron X-ray diffraction (SXRD) results further evidence the presence of metallic face-centered cubic (FCC) and body-centered cubic (BCC) phases, with no detectable retained oxides (**Fig. 2 C** and **D left**). Lattice constants of the FCC and the BCC phases are determined through Rietveld refinement as 3.60 Å and 2.87 Å, respectively. Even accounting for the uncertainties involved in different measurement techniques (*36*, *37*), these values are rationally larger than those of pure Ni (~3.52 Å) and pure Fe (~2.86 Å), serving as the first hint of substitutional alloying, which results from atomic scale mixing between Fe and Ni during synthesis (*38*). While bulk in its nature, our synthesized alloy is also excessively porous: a representative cross-sectional SE micrograph reveals a two-dimensional porosity of more than 27 % with worm-like alloy ligaments populating throughout the microstructure (**Fig. 2 D right**). These observations unambiguously support that the immense redox-catalyzed mass loss can be exploited to achieve bulk porous alloys, giving rise to reactive dealloying, as motivated in **Fig. 1 A** and **B**.

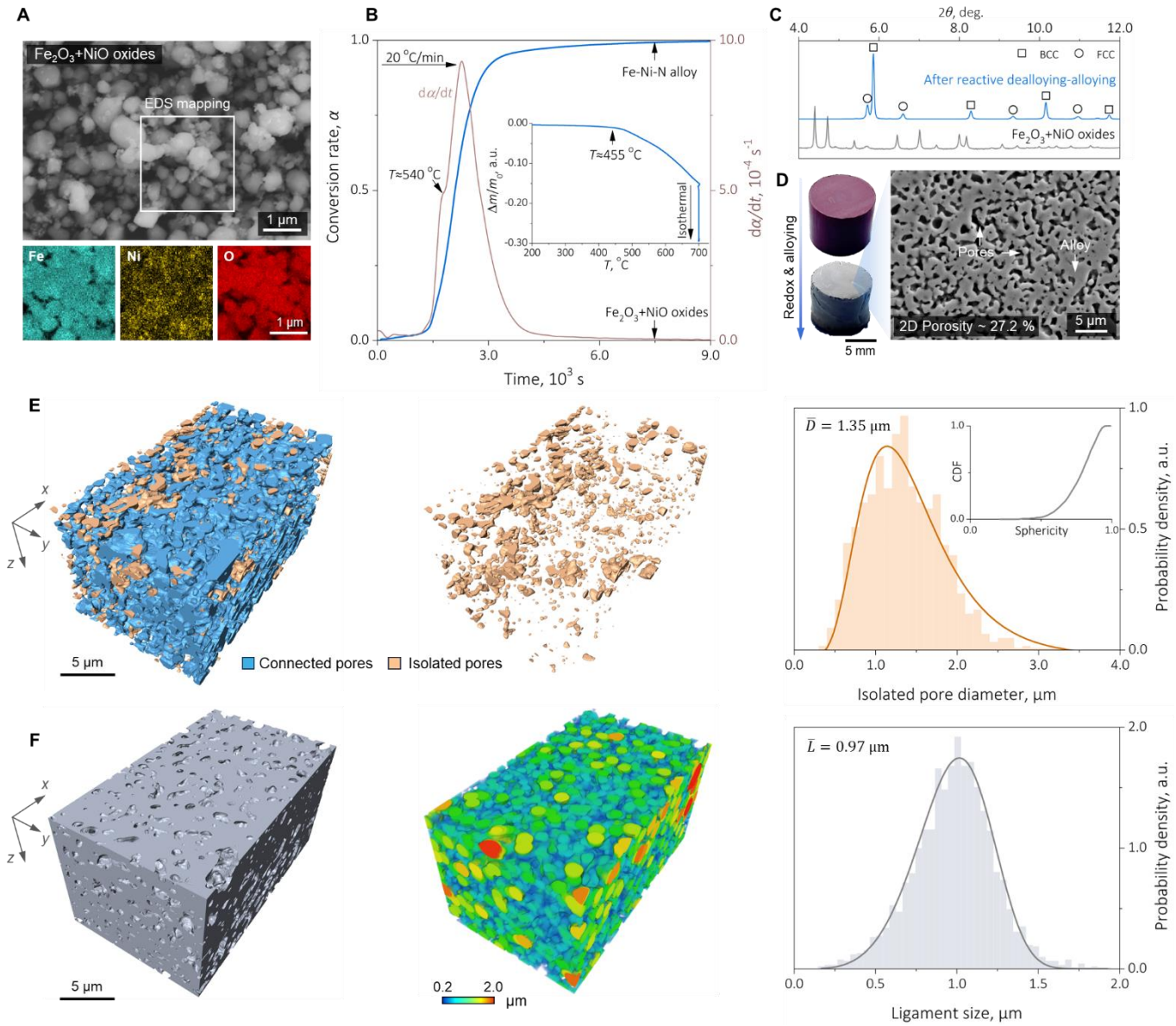

Figure 2 | Synthesis kinetics and three-dimensional nature of the porous alloy fabricated from Fe_2O_3 and NiO oxides. **(A)** SE micrograph and EDS maps for the Fe_2O_3 and NiO mixture. **(B)** Kinetic assessment for the synthesis process. Here, the global conversion rate $\alpha(t)$ has been calculated from the corresponding instantaneous mass loss, as described in the experimental section. The $\mathrm{d}\alpha/\mathrm{d}t$ curve is also determined, signifying the activation of more than one reactive dealloying micro-event and the inset of **(B)** shows that the mass loss incepts at ~455 °C. **(C)** *Ex-situ* SXRD profiles of the synthesized alloy and the mixed oxides. Only metallic FCC and BCC phases are present in the alloy specimen and no diffraction signals from retained oxides are present. **(D)** Macroscopic images of the synthesized bulk alloy and its oxide counterpart (left). The representative low-magnification SE micrograph (right) evidences the excessive porosity within the bulk alloy. **(E)** FIB-SEM-based tomography explorations of the pores. Left, the overall three-dimensional morphology of both the connected and the isolated pores. Middle, isolated pores. Right, statistical analysis of the isolated pore size (D) distribution, which follows a lognormal function: $\mathcal{F}(D) = \frac{1}{wD\sqrt{2\pi}}\exp\{-[\ln(D/\bar{D})]^2/2w^2\}$, where $\bar{D}$ denotes the mean isolated pore diameter. **(F)** Tomographic reconstruction of the alloy ligament. Left, the overall morphology. Middle, the computed ligament size. Right, the ligament size (L) distribution, as analyzed from a Weibull probability density function: $\mathcal{W}(L) = \frac{\kappa}{L}(\frac{L}{\lambda})^{\kappa-1}\exp(-\frac{L}{\lambda})^{\kappa}$, where κ and λ are the shape factor and the scaling factor, respectively. The mean ligament size, $\bar{L}$, is determined from $\bar{L} = \lambda\Gamma(1+\frac{1}{\kappa})$, where $\Gamma(x)$ is the gamma function: $\Gamma(x) = \int_0^{+\infty}\tau^{x-1}e^{-\tau}\mathrm{d}\tau$.

Focusing on the pores, we next performed focused-ion beam (FIB)-SEM-based tomography measurement to explore their three-dimensional characteristics. The reconstructed tomography micrographs confirm that the pores and the alloy ligaments are indeed interpenetrating in three dimensions (**Supplementary video 1**), giving rise to bi-continuous morphologies (*39*, *40*) (**Fig. 2 E left** and **F left**), in which the overall volumetric porosity reaches 28.9 % (**Fig. 2 E left**). Further connectivity quantification suggests that 94.1 % of the pores are connected while only 5.9 % of them are isolated (**Fig. 2 E middle** and **Supplementary video 2**). Such topological characteristics closely mimic nano-porous metals fabricated using the conventional chemical/electrochemical dealloying routes (*5*, *13*). Additionally, the massive, connected pores also hint at an evident kinetic decoupling between redox-catalyzed pore creation and surface energy-driven densification/structural coarsening (*41*), benefiting from the relatively low synthesis temperature ($< 0.75T_m$, T_m the bulk metal melting point). The equivalent diameter distribution of the isolated pores follows a lognormal function (**Fig. 2 E right**), where the mean diameter $\bar{D} = 1.35$ μm. The distribution of the alloy ligament size (**Fig. 2 F middle**), on the other hand, well aligns with a Weibull probability density function (*42*), and the mean ligament size $\bar{L} = 0.97$ μm (**Fig. 2 F right**). The fine ligament size together with the immense porosity is suggestive of prominent grain size refinement because of the Zener-like pinning effect (*43*), which motivates dedicated microstructural explorations detailed next, starting with the validation of substitutional alloying (**Fig. 1 A** and **C**).

Fig. 3 A showcases the coupled electron backscatter diffraction (EBSD)-EDS analyses of the as-synthesized porous alloys where a noticeably refined microstructure is evidenced: various sub-micrometer grains span over the alloy ligaments. An overall spatially homogenous distribution of Fe and Ni is seen across multiple grains (**Fig. 3 A bottom left**), directly confirming our conceived substitutional alloying process and the validity of the thermodynamic *treasure map* (**Fig. 1 C**). A closer inspection at the EBSD phase map and the inverse pole figure (IPF) next concludes the presence of three phases, including the

austenite (FCC, slightly enriched in Ni, **Fig. 3 A bottom left**), the nearly defect-free ferrite (BCC), and the highly-defected martensite. The presence of the martensite is rationalized by the reduced image quality in the phase map *(44)* (**Fig. 3 A top**), the high local kernel average misorientation value **(Supplementary Fig. S2)**, and the high defect density (**Fig. 3 A bottom right**). These observations fully confirm our alloy design concept that phase transformations are indeed unlocked by alloying (**Fig. 1 A**).

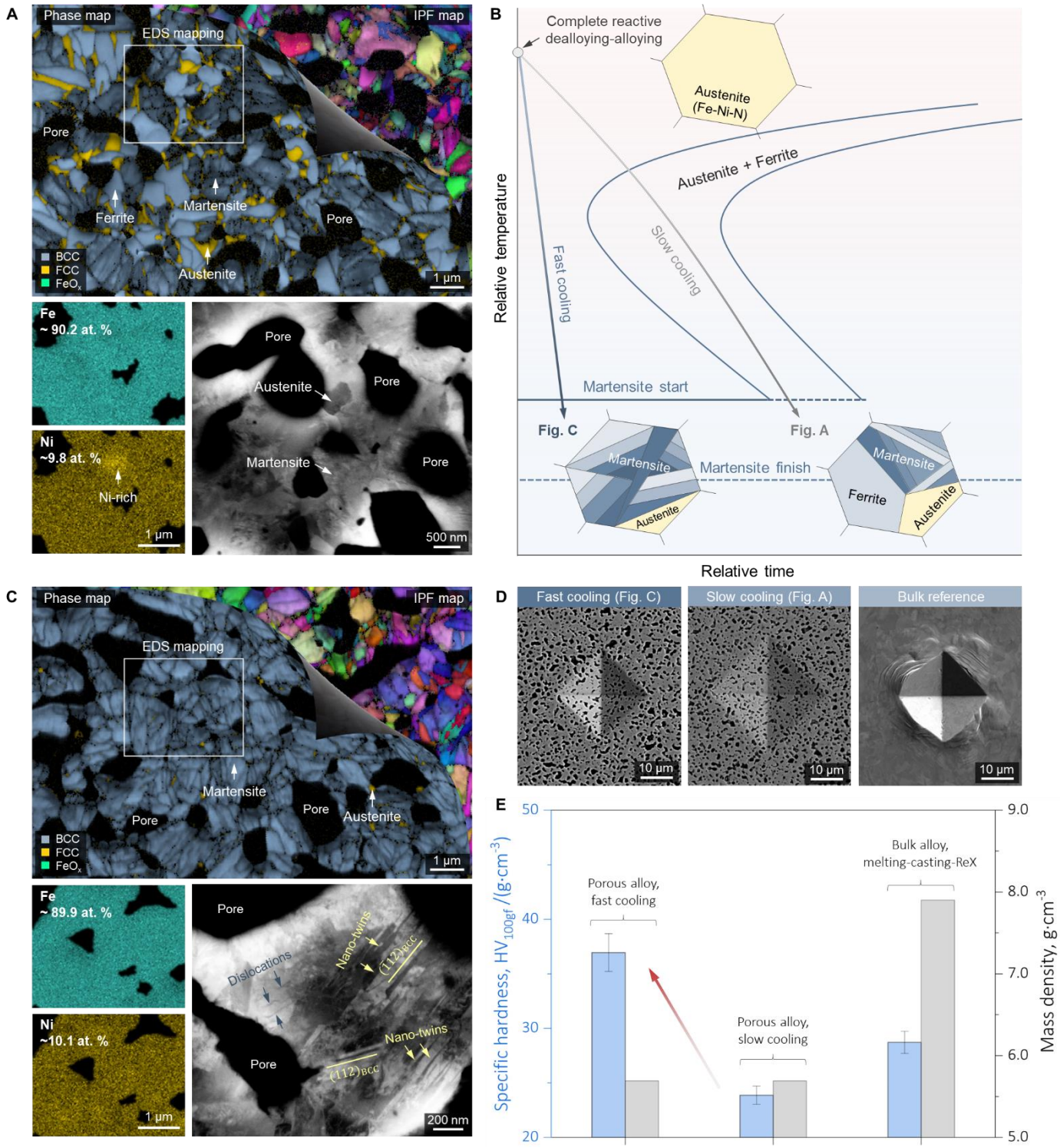

Figure 3 | Meso-scale microstructural analyses of the synthesized bulk nano-structured porous alloys. (A) Microstructural validation of substitutional alloying. Top, overlapped EBSD phase map and IPF map showing the presence of austenite, ferrite, and martensite. Bottom left, EDS maps taken across multiple grains confirming the overall spatially uniform distribution of Fe and Ni and the presence of local Ni enrichment at the austenite site. Bottom right, ECCI micrograph revealing the different defect densities in the austenite and the martensite. **(B)** Schematic of phase transformation pathway design. The three-phase microstructure in **(A)** suggests the possibility of achieving martensitic porous alloys by promoting the cooling rate.

(C) Microstructure of the porous martensitic alloy following the conceived phase transformation pathway in **(B)** Top, overlapped EBSD phase map and IPF map revealing the martensitic microstructure (multiple variants have been nucleated) with negligible retained austenite. Bottom left: EDS maps confirming the uniform distributions of Fe and Ni at the meso-scale. Bottom right: high-magnification ECCI micrograph validates the nano-structures within the martensite, in which a high number density of nano twins and dislocations are resolved. **(D)** and **(E)** Specific Vickers hardness and bulk mass density measurements of the martensitic porous alloy achieved from fast cooling (left of **(D)**), the prototypical three-phase porous alloy (middle of **(D)**), and the reference Fe-10 at.% Ni bulk alloy produced via the conventional melting-casting-recrystallization (ReX) route. More than seven Vickers hardness values were measured from each sample, and the error bars in **(E)** represent the standard deviations.

We note that the current microstructure achieved is to solely prove the design principle. That being stated, a broad spectrum of microstructural states is easily accessible, as sketched in **Fig. 3 B**, by fine tuning the phase transformation pathways. As a simple demonstrator case, we exemplify in **Fig. 3 C** the synthesis of a light-weight porous martensitic alloy, only by promoting the post-synthesis cooling rate with the aid of air quench. In distinctive contrast to **Fig. 3 A**, the entire microstructure almost fully consists of martensite, holding a Kurdjumov-Sachs orientation relationship *(45)* with its vicinal retained (parent) austenite (**Supplementary Fig. S3**), whose fraction barely exceeds 1.5 % (prior austenite grain size is only ~1.28 μm, **Supplementary Fig. S4**). As documented in the Wechsler-Lieberman-Read theory of martensite crystallography *(46)*, such a phase is nano-structured, largely due to the pronounced lattice invariant shear deformation involved. Our high magnification electron channeling contrast imaging (ECCI) micrograph further verifies this (**Fig. 3 C bottom right**): a high number density of $\{11\bar{2}\}\langle 111\rangle$ nano twins are seen (20~30 nm in thickness each) within the martensite accompanied by dislocations. Benefiting from the eminent defect strengthening contribution *(47)*, the porous martensitic alloy reveals a salient advantage in specific hardness (36.9 $HV_{100gf} \cdot g^{-1} \cdot cm^3$) over the as-synthesized porous alloy (23.9 $HV_{100gf} \cdot g^{-1} \cdot cm^3$) and its bulk Fe-10 at. % Ni counterpart (28.7 $HV_{100gf} \cdot g^{-1} \cdot cm^3$), while maintaining a low mass density of only 5.69 g/cm^3 (**Fig. 3 D** and **E**). Given the high specific hardness, the porous martensitic alloy also exhibits plastic deformability as no cracking or ligament micro-fracture is observed at any edges of the hardness indent (**Fig. 3 D**), motivating larger-scale high specific strength martensitic foam design as future work. While the demonstrator case discussed here in **Fig. 3** primarily targets miscible solid solution Fe-Ni-N porous alloys, in **Supplementary Fig. S5 and S6** we further validate our thermodynamic *treasure map* by demonstrating the synthesis of nitride-containing Fe-N and phase-separating Fe-Cu-N porous alloys.

Coming back to the overall alloy design scheme (**Fig. 1**), the only remaining pillar that necessities substantiation is interstitial alloying. We propose that the presence of martensitic transformation discussed in **Fig. 3** already serves as meso-scale evidence: such a beneficial phase transformation is only accessible when the porous alloys are synthesized in NH_3 (**Fig. 4 A left**), where N interstitials can be harvested from the vapor-phase, contributing to tetragonal distortion of the martensite *(48, 49)*. This principle can be easily generalized (see **Fig. 1A, top**) as also other types of martensite can be synthesized by exploiting alternative reactive vapor-phase constitution (*e.g.* CH_4, C_2H_2 or even their mixtures) that can dealloy oxygen and simultaneously donating an interstitial alloying element capable of triggering martensitic transformations. By contrast, a porous

alloy obtained when using H_2 alone as the reducing agent (see **Supplementary Fig. S7** for quantitative kinetic comparisons) and its bulk counterpart fabricated through the conventional melting-casting-recrystallization route both exhibit massive ferrite-like microstructures (*50*, *51*) (**Fig. 4 A middle** and **right**), even when the global Ni content and the cooling method were kept identical.

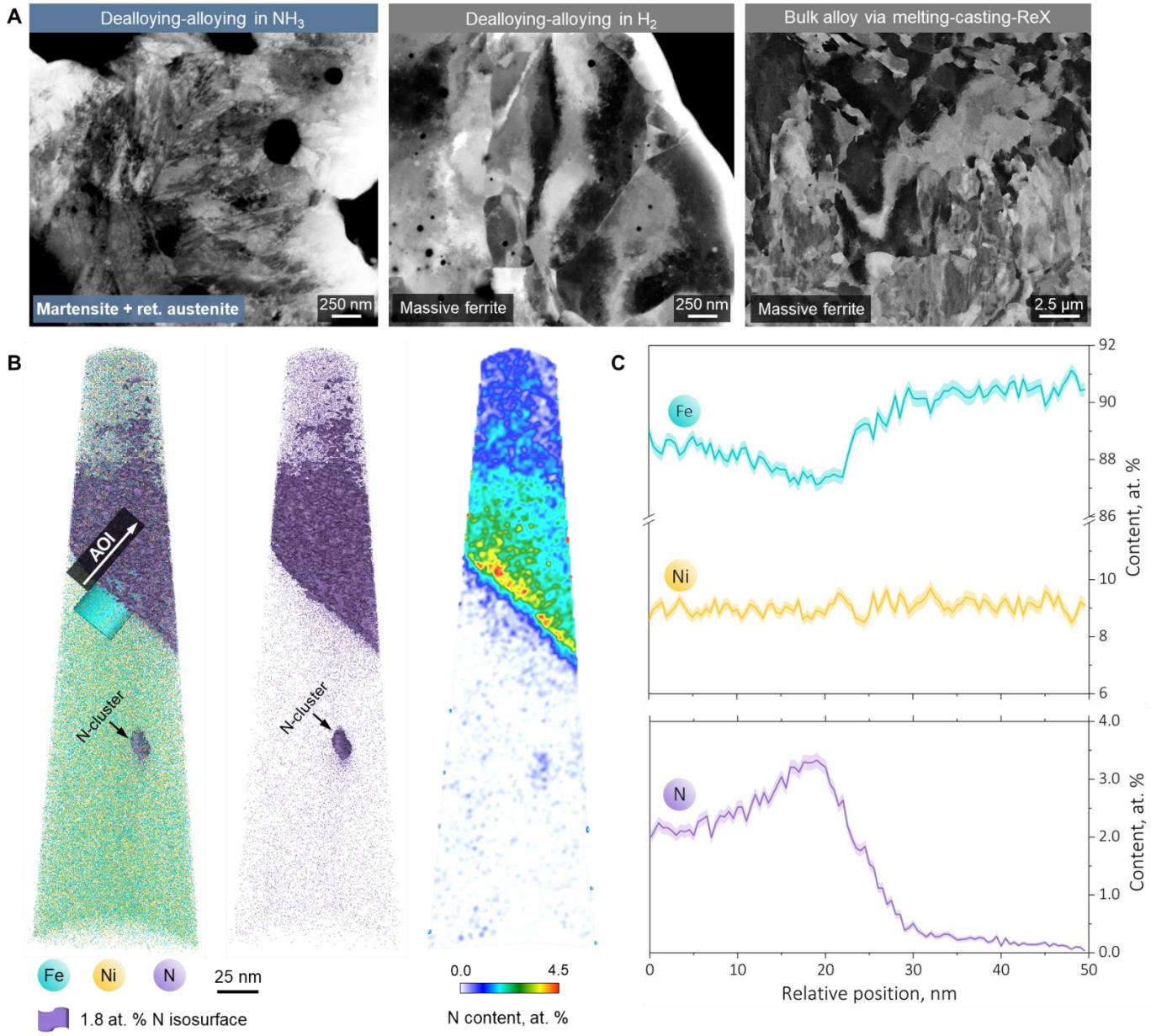

Figure 4 | Atomic-scale evidence of N interstitial alloying. (A) ECCI micrographs of three alloys with the same substitutional alloying element content (Fe-10 at.% Ni) but processed using different methods. Left and middle: dealloying-alloying synthesis with the reactive vapor-phase respectively chosen as pure NH_3 and pure H_2. Right: conventional melting-casting-recrystallization. It is seen that the desired martensitic microstructure is only available when NH_3 serves as the vapor phase constituent, the other two alloys both exhibit massive ferrite-like microstructures despite the cooling rates are kept identical in all three cases. **(B)** Three-dimensional APT measurements validating both Fe-Ni substitutional alloying and N interstitial alloying. Left: the overlapped Fe, Ni, and N distributions with an 1.8 at. % N isosurface highlighted. Middle: N distribution in which a nano-sized N cluster is also present (also see **Supplementary Fig. S8** for complementary analyses). Right: two-dimensional contour map of the N content, revealing the segregation possibly at planar defect sites within the martensite. **(C)** One dimensional Fe, Ni, and N distribution profiles acquired from the cylindrical area of interest sketched in **(B)**.

Zooming into the atomic scale, the presence of N interstitial (~0.41 at. % for the entire APT tip) is unequivocally confirmed by three-dimensional atom probe tomography (APT) measurements (**Fig. 4 B left**). Interestingly, N also reveals a certain

segregation tendency presumably at the planar defect sites within or at the vicinity of the martensite (**Fig. 4 B middle and right**), where the local N content reaches up to ~3.0 at. %, according to a cylindrical area of interest quantification (**Fig. 4 C**, also see **Supplementary Fig. S8** for complementary analyses). This sort of spatially inhomogeneous distribution of N introduces a new aspect to our alloy design scheme (**Fig. 1 A**), through segregation engineering (*52*), a well-recognized physical metallurgy approach to tailor the microstructure-property synergy. To ensure the reproducibility of the APT measurements, we have also carried out a separate set of measurements (**Supplementary Fig. S9**), in which the similar characteristics of N spatial distribution are also observed.

Having elaborated the possibility of harvesting interstitial N from the vapor-phase (**Fig. 4 B**), we emphasize that our proposed alloy design scheme may go far beyond the prototypical scope of solid solution alloy synthesis (**Fig. 1 C**), through which multiple metallic nitrides are also accessible (also supported by the presence of nitrides in **Supplementary Fig. S5** and **S6**). To substantiate this point and to also shed more quantitative light on the operating reactive dealloying-alloying micro-mechanisms, we opt for *in situ* SXRD measurements (details of the experimental instrument are provided in **Supplementary S10**), aiming to elaborate phase constitution change over time (**Supplementary video 3**). The progression of the reactions is visualized in **Fig. 5 A**, where stepwise redox pathways are significant, rationalizing the multiple inflection points seen in the global $\mathrm{d}\alpha/\mathrm{d}t$ curve (**Fig. 2 B**). By Rietveld refining the time-resolved diffractograms, it is recognized that the leading redox reaction $Fe_2O_3 \rightarrow Fe_3O_4$ is activated at ~440 ºC, followed by the $NiO \rightarrow Ni$ step, initiating at ~520 ºC (**Fig. 5 B** and also see **Fig. 5 C** as a guide to the eye). As a result, the relative phase fractions of Fe_2O_3 and NiO monotonically decrease, respectively diminishing at ~520 ºC and ~590 ºC, and their kinetics well complies the Boltzmann's sigmoidal function (*53*). The non-monotonic evolution observed in the Fe_3O_4 phase fraction, which peaks at ~0.87 in the 520-560 ºC temperature range, quantitatively confirms its presence as the intermediate step of the entire dealloying-alloying process. A minor transient metallic FCC phase (maximally ~0.02) is only momentarily present in the 480-530 ºC temperature range (**Figs. 5 B** and **C**), cross supporting the inception of substitutional alloying discussed in **Figs. 1** and **3**. This phase is further identified as pure Ni via lattice constant analysis, as revealed in **Supplementary Fig. S11**. Two predominant nitride phases, the γ'-$(Fe,Ni)_4N$ and the ε-Fe_3N/$(Fe,Ni)_3N$, respectively start to nucleate at ~500 ºC and ~580 ºC, achieving final equilibrium fractions of 0.48 and 0.52 during prolonged isothermal holding at 700 ºC for 1800 s (**Supplementary Fig. S12**). In **Supplementary Note 2** we also provide detailed rationalization for the unequivocal involvement of Ni substitutional alloying in driving phase transformations within the nitrides.

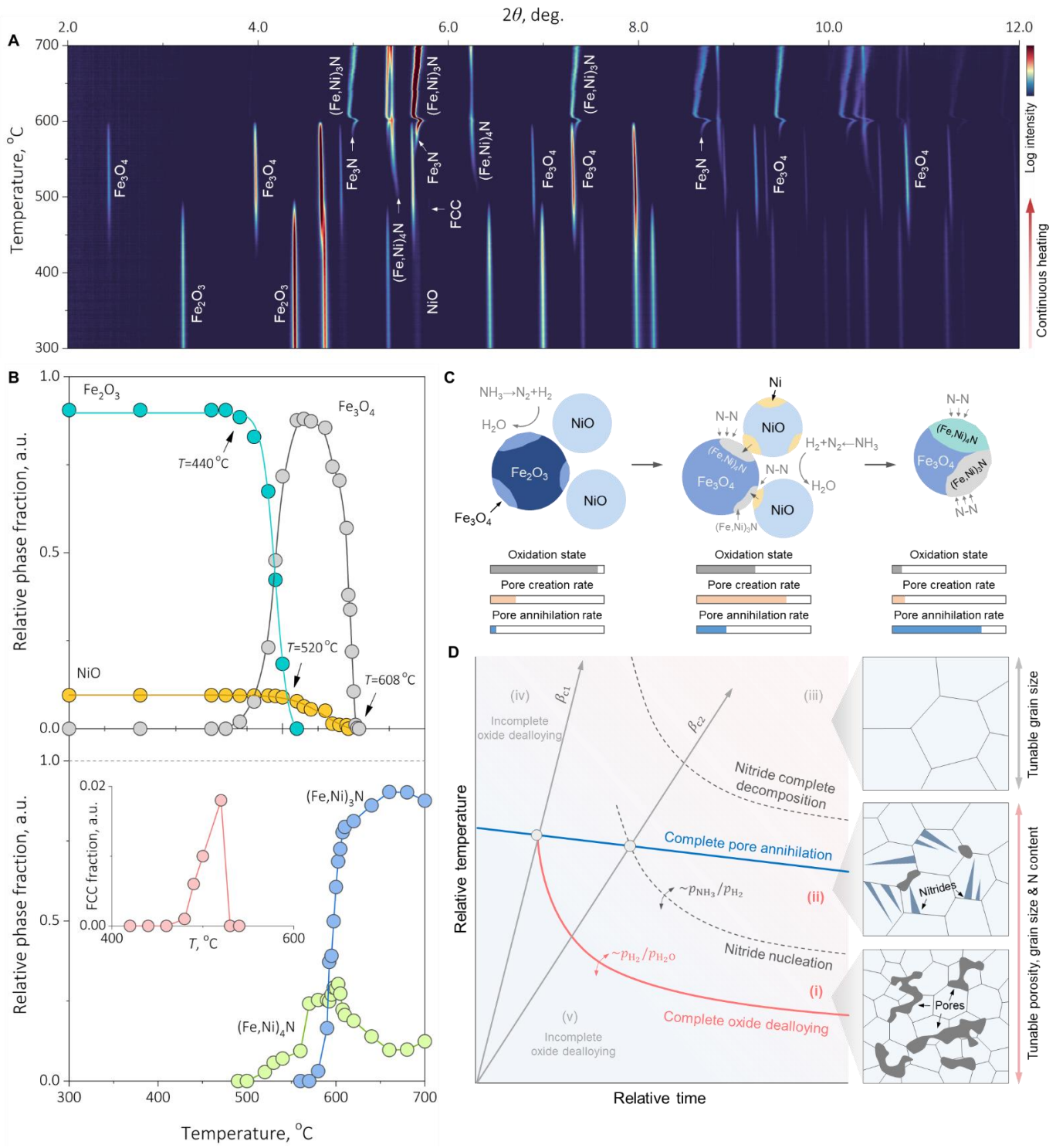

Figure 5 | *In situ* synchrotron X-ray explorations of the synthesis mechanisms and a kinetic conception for microstructural design. (A) Two-dimensional contour map revealing the progression of the dealloying-alloying process from which oxide dealloying and different nitrides are evidenced. **(B)** Relative phase fraction change as a function of temperature, quantified through Rietveld refinement. The relative phase fraction change of NiO and Fe_2O_3 over temperature aligns with the Boltzmann's sigmoidal function: $f(T) = f_f + (f_i - f_f)\left[1 + \exp\left(\frac{T-T_p}{dT}\right)\right]^{-1}$, where T_p denotes the temperature when $f = 0.5$ (489 °C for Fe_2O_3 and 557 °C for NiO), dT the rate factor (9.1 for Fe_2O_3 and 23.3 for NiO), f_i and f_f are the phase fractions at the initial and the final stage, respectively. We note that since all the redox reactions involve mass loss and the phase fraction of H_2O is unmeasurable via *in situ* SXRD, datum points in **(B)** cannot be used to back-calculate the absolute phase fraction or establish quantitative correlation with the thermogravimetry measurements. **(C)** Schematic of the synthesis mechanisms and the involvement of nitrides. Here, the extents of oxidation state, pore creation rate, and pore annihilation rate are also qualitatively sketched at various stages of the reaction. **(D)** An Ashby-type kinetic conception map qualitatively outlining the accessible microstructures. Regions (i) and (ii) reveal the kinetic window where tunable porosity, grain size, and different nitride states are possible. Regions (iii) represents significant microstructural coarsening after complete nitride

decomposition with fully densified microstructures. Regions (iv) and (v) denote incomplete oxide dealloying where immense amounts of oxides might still be retained in the microstructures.

All the foregoing observations and analyses not only validate the applicability and usefulness of the *thermodynamic treasure maps* proposed in **Fig. 1 B** and **C**, but also allow to derive an associated plausible Ashby-type of *kinetic* design guideline, as sketched in **Fig. 5 D**, qualitatively considering the interplays amongst *(i)* reactive oxide dealloying; *(ii)* pore creation/annihilation; and *(iii)* nitride nucleation/decomposition, which are the three most predominant mass transport micro-mechanisms identified earlier. Regions (i) and (ii) bounded by the oxide dealloying complete line (tunable via the redox potential *(19)* p_{H_2}/p_{H_2O}) and the complete pore annihilation line represent the most viable kinetic windows where tunable porosity and grain size are accessible. The dashed nitride nucleation line, which is also controllable by the nitriding potential *(15)* p_{NH_3}/p_{H_2}, serves as a switch to modulate between solid solution and nitride-containing microstructures. In contrast, process parameters surpassing the complete pore annihilation and the complete nitride decomposition lines (region (iii)) will instead only enable tunable grain size within the fully densified microstructures. While any quantitatively precise construction of such a *kinetic treasure map* still necessities extensive future efforts, the significance of heating rate can still be discussed, for which we hypothesize two critical values β_{c1} and β_{c2}, based on the microstructure states at the complete pore annihilation temperatures. The former represents the maximum possible heating rate for complete oxide dealloying, while the latter indicates the minimum heating rate to pursue full solid solution microstructures.

In summary, we reform the intuitive opposition between *alloying* and *dealloying* in metallurgical processing and introduce here an oxide-oriented metallic alloy design paradigm that encompasses vapor-phase reactive dealloying, substitutional alloying, interstitial alloying, phase transformations, and nano-structuring in one solid-state operation. Such an approach assigns all atoms from both reaction partners specific roles: H_2 from the NH_3 for oxygen removal in the reactive dealloying step, and N_2 for providing interstitials in the alloying step. We propose thermodynamic treasure maps that can quantitatively navigate the alloy synthesis in the profound composition-processing space and exemplify the synthesis of Fe-Ni-N bulk nano-structured porous martensitic alloys completely from oxides. Through dedicated multi-scale microstructural analyses and *in situ* diffractometry explorations of the governing redox and alloying micro-mechanisms, we also introduce an Ashby-type kinetic concept that unlocks microstructural design opportunities. The universality of our approach goes beyond the specific scope of porous solid solution synthesis, yet can be rather easily extended to: (i) bulk metallic nitride permanent magnetic alloys and (ii) alloy foam fabrication from oxide contaminated feedstocks or metallurgical wastes. Our alloy design paradigm also inspires future synergetic efforts amongst chemical synthesis, extractive, and physical metallurgy to turn oxides (or even minerals) directly into application-worthy products through diverse reactive vapor-phases.

Author contributions

S.L.W., Y.M., and D.R. conceived the project and designed the research; S.L.W. was the leading research scientist of this study, who carried out sample preparation, thermodynamic modelling, theoretical calculations, microscopy characterizations, property measurements, formulated the theories, and analyzed all the data; Y.M. performed the APT measurements, assisted the thermogravimetry test and the *in situ* synchrotron X-ray experiment; S.L.W. and D.R. rationalized the observations, wrote the manuscript, and prepared the contents shown in the supplementary information; D.R. coordinated all the research activities and hosted S.L.W. for the Alexander von Humboldt Research Fellowship. All authors discussed and approved the final version of the manuscript.

Acknowledgements

Synchrotron X-ray diffraction measurements were carried out at beamline P02.1, PETRA III of Deutsches Elektronen-Synchrotron (DESY, proposal Nos. I-20230183, I-20231121, and I-20231001). D.R. acknowledges funding by the European Union, through the project ROC, sponsored by the European Research Council (ERC, Grant No. 101054368). S.L.W. acknowledges financial support from MPG Scholarship and Alexander von Humboldt Research Fellowship (hosted by D.R.). The authors wish to thank Prof. Claudio Pistidda for providing the capillary reaction cell for *in situ* synchrotron X-ray experiments. Thanks are also due to Mr. Tianyi You for the artwork of Fig. 1 (A). Dr.-Ing. Tim Schwarz, Mr. Chengguang Wu, and Ms. Xizhen Dong are also acknowledged for the technical support on APT sample preparation and data analysis. S.L.W. thanks Dr. Guillaume Hachet for the valuable discussion on the theories of alloying.

References

1. G. Masing, Zur Theorie der Resistenzgrenzen in Mischkristallen. *Zeitschrift für Anorg. und Allg. Chemie* (1921), doi:10.1002/zaac.19211180127.
2. J. Erlebacher, M. J. Aziz, A. Karma, N. Dimitrov, K. Sieradzki, Evolution of nanoporosity in dealloying. *Nature* (2001), doi:10.1038/35068529.
3. C. Zhu, Z. Qi, V. A. Beck, M. Luneau, J. Lattimer, W. Chen, M. A. Worsley, J. Ye, E. B. Duoss, C. M. Spadaccini, C. M. Friend, J. Biener, Toward digitally controlled catalyst architectures: Hierarchical nanoporous gold via 3D printing. *Sci. Adv.* (2018), doi:10.1126/sciadv.aas9459.
4. Y. Li, B. N. Ngo-Dinh, J. Markmann, J. Weissmüller, Evolution of length scales and of chemical heterogeneity during primary and secondary dealloying. *Acta Mater.* (2022), doi:10.1016/j.actamat.2021.117424.
5. J. Weissmüller, K. Sieradzki, Dealloyed nanoporous materials with interface-controlled behavior. *MRS Bull.* (2018), doi:10.1557/mrs.2017.299.
6. D. Raabe, The Materials Science behind Sustainable Metals and Alloys. *Chem. Rev.* (2023), , doi:10.1021/acs.chemrev.2c00799.
7. L. Brewer, The thermodynamic properties of the oxides and their vaporization processes. *Chem. Rev.* (1953), doi:10.1021/cr60161a001.
8. B. C. H. Steele, Oxygen transport and exchange in oxide ceramics. *J. Power Sources* (1994), doi:10.1016/0378-7753(93)01789-K.
9. J. S. Lim, H. H. Nahm, M. Campanini, J. Lee, Y. J. Kim, H. S. Park, J. Suh, J. Jung, Y. Yang, T. Y. Koo, M. D. Rossell, Y. H. Kim, C. H. Yang, Critical ionic transport across an oxygen-vacancy ordering transition. *Nat. Commun.* (2022), doi:10.1038/s41467-022-32826-8.

10. Y. Dong, Redox enhanced slow ion kinetics in oxide ceramics. *J. Am. Ceram. Soc.* (2024), doi:10.1111/jace.19441.
11. P. Cavaliere, L. Dijon, A. Laska, D. Koszelow, Hydrogen direct reduction and reoxidation behaviour of high-grade pellets. *Int. J. Hydrogen Energy* (2023), doi:10.1016/j.ijhydene.2023.08.254.
12. S. H. Kim, X. Zhang, Y. Ma, I. R. Souza Filho, K. Schweinar, K. Angenendt, D. Vogel, L. T. Stephenson, A. A. El-Zoka, J. R. Mianroodi, M. Rohwerder, B. Gault, D. Raabe, Influence of microstructure and atomic-scale chemistry on the direct reduction of iron ore with hydrogen at 700°C. *Acta Mater.* (2021), doi:10.1016/j.actamat.2021.116933.
13. I. McCue, E. Benn, B. Gaskey, J. Erlebacher, Dealloying and Dealloyed Materials. *Annu. Rev. Mater. Res.* (2016), , doi:10.1146/annurev-matsci-070115-031739.
14. E. J. Mittemeijer, *Fundamentals of Materials Science* (2021).
15. E. J. Mittemeijer, M. A. J. Somers, *Thermochemical Surface Engineering of Steels: Improving Materials Performance* (2014).
16. N. Yasuda, Y. Mochizuki, N. Tsubouchi, T. Akiyama, Reduction and nitriding behavior of hematite with ammonia. *ISIJ Int.* (2015), doi:10.2355/isijinternational.55.736.
17. T. Furuhara, Y. Zhang, M. Sato, G. Miyamoto, M. Enoki, H. Ohtani, T. Uesugi, H. Numakura, Sublattice alloy design of high-strength steels: Application of clustering and nanoscale precipitation of interstitial and substitutional solutes. *Scr. Mater.* (2023), doi:10.1016/j.scriptamat.2022.115063.
18. T. Fujita, P. Guan, K. McKenna, X. Lang, A. Hirata, L. Zhang, T. Tokunaga, S. Arai, Y. Yamamoto, N. Tanaka, Y. Ishikawa, N. Asao, Y. Yamamoto, J. Erlebacher, M. Chen, Atomic origins of the high catalytic activity of nanoporous gold. *Nat. Mater.* (2012), doi:10.1038/nmat3391.
19. C. H. P. Lupis, *Chemical Thermodynamics of Materials* (Prentice Hall, 1993).
20. A. T. Dinsdale, SGTE data for pure elements. *Calphad* (1991), doi:10.1016/0364-5916(91)90030-N.
21. W. F. Gale, T. C. Totemeier, *Smithells Metals Reference Book* (2003).
22. C. Cai, S. Wei, Z. Yin, J. Bai, W. Xie, Y. Li, F. Qin, Y. Su, D. Wang, Oxygen vacancy formation and uniformity of conductive filaments in Si-doped Ta2O5 RRAM. *Appl. Surf. Sci.* **560**, 149960 (2021).
23. R. Chatten, A. V. Chadwick, A. Rougier, P. J. D. Lindan, The oxygen vacancy in crystal phases of WO3. *J. Phys. Chem. B.* **109**, 3146–3156 (2005).
24. Y. Hinuma, T. Toyao, T. Kamachi, Z. Maeno, S. Takakusagi, S. Furukawa, I. Takigawa, K. I. Shimizu, Density Functional Theory Calculations of Oxygen Vacancy Formation and Subsequent Molecular Adsorption on Oxide Surfaces. *J. Phys. Chem. C.* **122**, 29435–29444 (2018).
25. A. H. Heuer, T. Nakagawa, M. Z. Azar, D. B. Hovis, J. L. Smialek, B. Gleeson, N. D. M. Hine, H. Guhl, H. S. Lee, P. Tangney, W. M. C. Foulkes, M. W. Finnis, On the growth of Al2O3 scales. *Acta Mater.* **61**, 6670–6683 (2013).
26. Y. C. Zhang, L. Pan, J. Lu, J. Song, Z. Li, X. Zhang, L. Wang, J. J. Zou, Unraveling the facet-dependent and oxygen vacancy role for ethylene hydrogenation on Co 3 O 4 (110) surface: A DFT+U study. *Appl. Surf. Sci.* **401**, 241–247 (2017).
27. H. Jabraoui, M. Djafari Rouhani, C. Rossi, A. Esteve, First-principles investigation of CuO decomposition and its transformation into Cu2 O. *Phys. Rev. Mater.* **6**, 1–9 (2022).
28. A. J. R. Hensley, Y. Wang, J. S. McEwen, The partial reduction of clean and doped A-Fe2O3(0001) from first principles. *Appl. Catal. A Gen.* **582**, 116989 (2019).
29. U. Aschauer, N. Vonrüti, N. A. Spaldin, Effect of epitaxial strain on cation and anion vacancy formation in MnO. *Phys. Rev. B - Condens. Matter Mater. Phys.* **92**, 1–5 (2015).
30. W. B. Zhang, N. Yu, W. Y. Yu, B. Y. Tang, Stability and magnetism of vacancy in NiO: A GGA+U study. *Eur. Phys. J. B.* **64**, 153–158 (2008).
31. A. Takeuchi, A. Inoue, Classification of bulk metallic glasses by atomic size difference, heat of mixing and period of constituent elements and its application to characterization of the main alloying element. *Mater. Trans.* (2005), doi:10.2320/matertrans.46.2817.
32. L. Holappa, M. Kekkonen, A. Jokilaakso, J. Koskinen, A Review of Circular Economy Prospects for Stainless Steelmaking Slags. *J. Sustain. Metall.* (2021), , doi:10.1007/s40831-021-00392-w.
33. Y. Ma, J. W. Bae, S. Kim, M. Jovi˘, K. Li, D. Vogel, D. Ponge, M. Rohwerder, B. Gault, D. Raabe, Reducing Iron Oxide with Ammonia: A Sustainable Path to Green Steel. *Adv. Sci.* **2300111**, 1–7 (2023).
34. R. K. Pathria, P. D. Beale, *Statistical Mechanics, Third Edition* (2007).
35. D. G. Löffler, L. D. Schmidt, Kinetics of NH3 decomposition on iron at high temperatures. *J. Catal.* (1976), doi:10.1016/0021-9517(76)90395-X.

36. E. R. Jette, F. Foote, Precision determination of lattice constants. *J. Chem. Phys.* (1935), doi:10.1063/1.1749562.
37. M. Yousuf, P. C. Sahu, H. K. Jajoo, S. Rajagopalan, K. G. Rajan, Effect of magnetic transition on the lattice expansion of nickel. *J. Phys. F Met. Phys.* (1986), doi:10.1088/0305-4608/16/3/015.
38. L. Vegard, Die Konstitution der Mischkristalle und die Raumfüllung der Atome. *Zeitschrift für Phys.* (1921), doi:10.1007/BF01349680.
39. C. Soyarslan, S. Bargmann, M. Pradas, J. Weissmüller, 3D stochastic bicontinuous microstructures: Generation, topology and elasticity. *Acta Mater.* (2018), doi:10.1016/j.actamat.2018.01.005.
40. Z. Lu, C. Li, J. Han, F. Zhang, P. Liu, H. Wang, Z. Wang, C. Cheng, L. Chen, A. Hirata, T. Fujita, J. Erlebacher, M. Chen, Three-dimensional bicontinuous nanoporous materials by vapor phase dealloying. *Nat. Commun.* (2018), doi:10.1038/s41467-017-02167-y.
41. S. J. L. Kang, *Sintering: Densification, grain growth and microstructure* (2005).
42. A. J. Hallinan, A Review of the Weibull Distribution. *J. Qual. Technol.* (1993), doi:10.1080/00224065.1993.11979431.
43. E. Nes, N. Ryum, O. Hunderi, On the Zener Drag. *Acta Mater.* **33**, 11–22 (1985).
44. S. Zaefferer, N. N. Elhami, P. Konijnenberg, "Electron backscatter diffraction (EBSD) techniques for studying phase transformations in steels" in *Phase Transformations in Steels* (2012).
45. J. H. van der Merwe, G. J. Shiflet, The role of structural ledges at phase boundaries-III. F.C.C.-B.C.C. interfaces in Kurdjumov-Sachs orientation. *Acta Metall. Mater.* (1994), doi:10.1016/0956-7151(94)90136-8.
46. M. S. Wechsler, On the theory of martensitic transformations. The generalized lattice invariant shear and the degeneracy of solutions for the cubic to tetragonal transformation. *Acta Metall.* **7**, 793–802 (1959).
47. A. Argon, *Strengthening Mechanisms in Crystal Plasticity* (2007), vol. 9780198516.
48. V. A. Lobodyuk, Y. Y. Meshkov, E. V. Pereloma, On Tetragonality of the Martensite Crystal Lattice in Steels. *Metall. Mater. Trans. A Phys. Metall. Mater. Sci.* (2019), doi:10.1007/s11661-018-4999-z.
49. D. T. Keating, A. N. Goland, Atomic displacements in iron martensite. *Acta Metall.* (1967), doi:10.1016/0001-6160(67)90045-4.
50. A. Borgenstam, M. Hillert, Massive transformation in the Fe-Ni system. *Acta Mater.* (2000), doi:10.1016/S1359-6454(00)00102-6.
51. T. B. Massalski, "Massive transformations revisited" in *Metallurgical and Materials Transactions A: Physical Metallurgy and Materials Science* (2002).
52. D. Raabe, M. Herbig, S. Sandlöbes, Y. Li, D. Tytko, M. Kuzmina, D. Ponge, P. P. Choi, Grain boundary segregation engineering in metallic alloys: A pathway to the design of interfaces. *Curr. Opin. Solid State Mater. Sci.* (2014), , doi:10.1016/j.cossms.2014.06.002.
53. S. Wei, J. Kang, C. C. Tasan, An in situ synchrotron X-ray study of reverse austenitic transformation in a metastable FeMnCo alloy. *J. Mater. Res.*, 1–16 (2022).